Metallicity Gradients in Modern Cosmological Simulations II: The Role of Bursty Versus Smooth Feedback at High Redshift

Alex M. Garcia [ID],[1,2,3] Paul Torrey [ID],[1,2,3] Aniket Bhagwat [ID],[4] Xuejian Shen [ID],[5] Mark Vogelsberger [ID],[5] William McClymont [ID],[6,7] Peixin Zhu [ID],[8] Dhruv T. Zimmerman [ID],[9] Oliver Zier [ID],[8] Sarah Biddle [ID],[8] Ruby J. Wright [ID],[10] Kathryn Grasha [ID],[11,*] Laura Keating [ID],[12] Benedetta Ciardi,[4] Lars Hernquist [ID],[8] and et al.

[1] *Department of Astronomy, University of Virginia, 530 McCormick Road, Charlottesville, VA 22904*

[2] *Virginia Institute for Theoretical Astronomy, University of Virginia, Charlottesville, VA 22904, USA*

[3] *The NSF-Simons AI Institute for Cosmic Origins, USA*

[4] *Max Planck Institut für Astrophysik, Karl Schwarzschild Straße 1, D-85741 Garching, Germany*

[5] *Department of Physics and Kavli Institute for Astrophysics and Space Research, Massachusetts Institute of Technology, Cambridge, MA 02139, USA*

[6] *Kavli Institute for Cosmology, University of Cambridge, Madingley Road, Cambridge CB3 0HA, UK*

[7] *Cavendish Laboratory, University of Cambridge, 19 JJ Thomson Avenue, Cambridge CB3 0HE, UK*

[8] *Harvard-Smithsonian Center for Astrophysics, 60 Garden Street, Cambridge, MA 02138, USA*

[9] *Department of Astronomy, University of Florida, 211 Bryant Space Sciences Center, Gainesville, FL 32611 USA*

[10] *International Centre for Radio Astronomy Research (ICRAR), M468, University of Western Australia, 35 Stirling Hwy, Crawley, WA 6009, Australia*

[11] *Research School of Astronomy and Astrophysics, Australian National University, Canberra, ACT 2611, Australia*

[12] *Institute for Astronomy, University of Edinburgh, Blackford Hill, Edinburgh, EH9 3HJ, UK*

ABSTRACT

The spatial distribution of gas-phase metals within galaxies is highly sensitive to the underlying physics governing galaxy evolution. Stellar feedback is one such driver that can radially redistribute metals throughout the entire galaxy. The sensitivity of the metal content to feedback is especially pronounced at high redshift when galaxies are rapidly assembling. In this work, we investigate the radial gas-phase metallicity gradients at high redshift ($3 < z \lesssim 11$) in the FIRE-2, SPICE, and Thesan cosmological simulations, which span a variety of different feedback implementations with both bursty (i.e., time variable) and smooth stellar feedback implementations. We find that the metallicity gradients in the bursty feedback models (FIRE, Thesan Zoom, and SPICE Bursty) show systematically flatter gradients than the smooth feedback models (Thesan Box and SPICE Smooth). The difference is most clear in massive galaxies ($M_\star > 10^9$ $M_\odot$), while lower mass galaxies have weaker discrepancies. We then contextualize our results with the first paper of this series to show the chemical evolutionary history of galaxies across $\gtrsim 13$ Gyr in modern cosmological simulations. Finally, we compare with recent observations, finding that the majority – but, notably, not all – of the observed gradients favor a bursty feedback scenario, highlighting the utility of metallicity gradients as probes of feedback physics at high redshift.

1. INTRODUCTION

Feedback is central to galaxy evolution, but capturing its impact on galaxies remains a major challenge for simulations. Stars are among the most important sources of feedback, driving it through multiple channels including supernovae, photoionization and radiation pressure, protostellar jets, and stellar winds (e.g., Jijina & Adams 1996; Yorke et al. 1989; Dale et al. 2005; Quillen et al. 2005; Evans et al. 2009; Lopez et al. 2011). These processes can influence galaxies on large scales, yet modern galaxy evolution simulations lack the resolution to capture the small-scale physics where stellar feedback originates and operates. Nonetheless, accurately model-

Corresponding author: Alex M. Garcia

alexgarcia@virginia.edu

* ARC DECRA Fellow

ing feedback on these unresolved scales is imperative to producing realistic galaxy populations.

At present, galaxy evolutionary simulations that model baryonic feedback can be broadly categorized as either: (i) high-resolution zoom-in simulations of individual galaxies and their local environment ($\sim$a few Mpc scales) and (ii) lower-resolution large ($\gtrsim 35 - 300$ Mpc scales) cosmological box simulations (see Vogelsberger et al. 2020, for a review). High-resolution simulations (e.g. FIRE Hopkins et al. 2014; or SMUGGLE Marinacci et al. 2019) can begin to resolve the multiphase ISM down to approximately giant molecular cloud ($M_{baryon} \lesssim 10^4$ M$_\odot$) scales, allowing for explicit modeling of star formation, feedback, and cooling. Such simulations have been successful at reproducing a number of galactic-scale properties (El-Badry et al. 2016; Sparre et al. 2017; Ma et al. 2017; Torrey et al. 2017, etc.). However, owing to the high computational cost, it is difficult to produce large samples of galaxies across a variety of cosmological environments (although, see recent efforts by FIREbox, Feldmann et al. 2023, and COLIBRE, Schaye et al. 2025).

Lower-resolution large-box simulations, on the other hand, provide a large population of galaxies in a wide diversity of environments (Vogelsberger et al. 2014; Schaye et al. 2015; Davé et al. 2019; Pillepich et al. 2018, etc.). The cosmological box simulations have had their share of success reproducing population-level scaling relationships (Agertz et al. 2011; Genel et al. 2014; Sparre et al. 2015; Ferrero et al. 2017; Davé et al. 2019; Torrey et al. 2019, etc.). A downside for these models, though, is that the scales of star formation, and the resultant feedback, are entirely unresolved. These processes are therefore usually treated entirely as phenomenological prescriptions. Typical treatments rely on simplifying assumptions, such as describing the behavior of the dense, star-forming ISM with an effective equation of state (e.g., Springel & Hernquist 2003; Schaye & Dalla Vecchia 2008) or temporarily decoupling feedback-driven winds from the hydrodynamics to help facilitate the escape of gas (Vogelsberger et al. 2013; Davé et al. 2019).

A key consequence of different treatments of star formation and feedback is that the star formation histories of galaxies in explicit models are much more bursty (strongly time variable) than those of equation of state ISM models. The bursty nature of the feedback from explicit models comes from their self-regulation of the star-forming ISM. While an equation of state provides additional pressure support that prevents the collapse of all gas into stars (Springel & Hernquist 2003; Schaye & Dalla Vecchia 2008), such pressure support is not included out-of-the-box in explicit ISM models. Therefore,
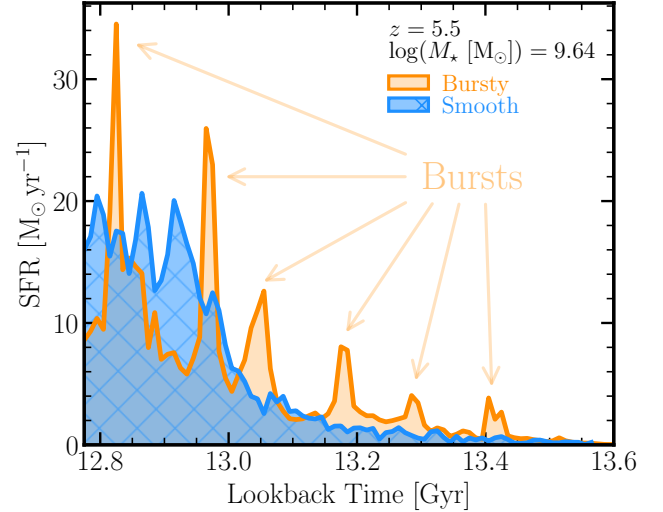

Figure 1. Example Star Formation Histories in Bursty and Smooth Feedback Models. The mass assembly of two galaxies with stellar mass $\log(M_\star$ [M$_\odot$]$) = 9.64$ at $z \sim 5.5$ from Thesan Zoom (bursty) and Thesan Box (smooth). The bursty model has episodic factors of a few increases in star formation rates. These bursts of star formation lead directly to bursts of feedback. While the "smooth" models do still have time variations of their star formation rates, the variation is on the order of a few 10%. Finally, we note that these galaxies were selected purely on stellar mass at $z = 5.5$ and are not the same halo run with different models.

the treatment of feedback needs to prevent all of the local gas from converting into stars. This explicit self-regulation by feedback from stars leads to an episodic nature of star formation followed by rapid quenching.

To put this more concretely, we show two example star formation histories in Figure 1 for two galaxies of the same stellar mass at $z \sim 5.5$ in Thesan Box and Thesan Zoom project (Kannan et al. 2022 2025; simulations described in more detail in Section 2.1.3). The explicit ISM model (labeled bursty) has several bursts of star formation (rapid enhancements and decreases of factors of a few), while the equation of state ISM (labeled smooth) model has a much smoother star formation history.[1] The bursts of star formation lead directly to episodic blow-outs of gas as large populations of massive stars formed during the burst die concurrently, thereby preventing further local star formation (Muratov et al. 2015, 2017; Anglés-Alcázar et al. 2017; Pandya et al. 2021).

---

[1] It should be noted that the "smooth" star formation does still have time variation; however, it is on the tens of percent level, unlike the factors of several in bursty models.

One advantage of bursty feedback is that it can naturally be invoked to alleviate small-scale tensions with ΛCDM, such as the core-cusp problem (Read & Gilmore 2005; Pontzen & Governato 2012; Lazar et al. 2020; Mostow et al. 2024) by driving rapid fluctuations of the gravitational potential, and the overabundance of UV bright galaxies at high-redshift (e.g., Shen et al. 2023, 2024a; Sun et al. 2023; Narayanan et al. 2024a) with bursts contributing to a high fraction of the UV luminosity. Bursts are therefore not just a unique modeling quirk of high-resolution simulations, but a potentially necessary ingredient in galaxy evolution (see also Looser et al. 2024; Danhaive et al. 2025; McClymont et al. 2025a,b; Witten et al. 2025, etc). It is not fully clear at present, however, the imprints of these systematic and episodic blowouts are on the rest of the galaxy.

A method by which the effect of rapid, large outflows triggered by star formation can be quantified is by looking at the overall metal content, or metallicity, of the galaxy (see, e.g., work by Garcia et al. 2023, 2024a,b, 2025a,b; Bassini et al. 2024; Marszewski et al. 2025; McClymont et al. 2025b). Metals are ideal as they produce bright emission lines that can be easily observed in the (rest) optical (Kewley et al. 2019; Maiolino & Mannucci 2019) while tracing the flows and chemical enrichment of the system (Tumlinson et al. 2017; Muratov et al. 2017; Péroux & Howk 2020). Metallicity thus offers an observable, *direct* probe of how feedback regulates galaxies' growth and evolution. The spatial distribution of metals within galaxies traces the system's assembly and evolution, making it a particularly useful tool.

Local galaxies generally exhibit higher metallicities in their centers than their outskirts, a pattern usually characterized by a negative (radially decreasing) metallicity gradient (Searle 1971; Sánchez et al. 2013; Stanghellini et al. 2015; Franchetto et al. 2021; Nelson et al. 2021). The existence of negative gradients is usually explained with inside-out galaxy growth, wherein the stellar populations in the center of the galaxy form and evolve earlier than on the outskirts, chemically enriching the inner regions earlier (e.g., Prantzos & Boissier 2000; Pilkington et al. 2012; Pérez et al. 2013; Tissera et al. 2019). The characteristic negative gradients can be flattened (perhaps even inverted) by radial mixing within the disk via winds (Gibson et al. 2013; Ma et al. 2017; Garcia et al. 2023), gas flows along spiral arms (Friedli et al. 1994; Friedli & Benz 1995; Orr et al. 2023), mergers (Rupke et al. 2010a,b; Torrey et al. 2012) or through pristine gas inflows into the central regions of galaxies (Ceverino et al. 2016; Tissera et al. 2022; Rodríguez Del Pino et al. 2024; Tapia-Contreras et al. 2025). Moreover, the host mass of a galaxy has been shown to be important for metallicity gradients, both in simulations and observations (Belfiore et al. 2017; Garcia et al. 2025b). As such, a wide variety of negative, flat, and positive gradients are observed across time (e.g., Wuyts et al. 2016; Wang et al. 2017, 2019, 2020; Curti et al. 2020; Simons et al. 2021; Grasha et al. 2022; Valé et al. 2025), although observational systematics (e.g., limited angular resolution) can also have systematic impacts on measured gradients (see, e.g., Yuan et al. 2013; Acharyya et al. 2020).

In Garcia et al. (2025b), we show that modern large volume cosmological simulations are in tension with high redshift ($z > 3$) observations of metallicity gradients (Troncoso et al. 2014; Wang et al. 2022; Arribas et al. 2024; Tripodi et al. 2024; Vallini et al. 2024; Venturi et al. 2024). We find that EAGLE (Schaye et al. 2015), Illustris (Vogelsberger et al. 2014), IllustrisTNG (Pillepich et al. 2018), and SIMBA (Davé et al. 2019) – notably all effective equation of state ISM models – produce systematically stronger gradients (i.e., more negative) than are observed at $z > 3$, especially in intermediate-to-high mass galaxies (10^9 M$_\odot$ < $M_\star$ < 10^{10} M$_\odot$), suggesting that these models do not mix their gas content sufficiently. Since that work, there have been a few more gradients measured at high redshift with *JWST* at $z \gtrsim 3$ (Acharyya et al. 2024; Ivey et al. 2025; Li et al. 2025). While Li et al. (2025) presents some evidence for strong negative gradients at high redshift, the preference for flat gradients at high redshift persists. If galaxies truly do have systematically flat gradients at high redshift, then many modern cosmological simulations do not accurately model galaxy formation in its earliest stages.

Stellar feedback plays a central role in the evolution of metallicity gradients. Gibson et al. (2013) shows, using the MUGS (Stinson et al. 2010) and MaGICC (Brook et al. 2012) models, that feedback variations can lead to qualitatively different behavior of metallicity gradients. They find that the enhanced feedback models of MaGICC lead to systematically flatter gradients than the more conservative MUGS model. Inspired by the results of Gibson et al. (2013) – and continuing the effort started in Garcia et al. (2025b) – we aim here to quantify the role of *bursty* feedback in resolving the metallicity gradient tension at high redshift. Specifically, we place both smooth and bursty models on an even footing to provide a unique vantage point for viewing the impact of these models.

The rest of this paper is arranged as follows. In Section 2, we introduce the simulation models we analyze in this work, define our galaxy selection criteria, and then describe our methodology for calculating metallicity gradients. In Section 3, we show the full distribution

of high redshift ($3 < z \lesssim 11$) gradients in each simulation and then break our samples into both stellar mass and redshift bins. In Section 4, we contextualize the results of this work and Garcia et al. (2025b) to present a complete picture of the gas-phase metallicity gradient evolution over 13 billion years in cosmological simulations and compare to recent observational results at high redshift ($z > 3$). Finally, in Section 5, we state our conclusions.

2. METHODS

We employ data products from the FIRE, SPICE, and Thesan cosmological simulations. The advantage of these models for this work is that they offer an assortment of physical implementations, both bursty and smooth stellar feedback. Moreover, each of these models includes simulations of massive galaxies ($M_\star \gtrsim 10^8$ M$_\odot$) in the early universe ($z \gtrsim 5$), allowing us to probe the earliest onset of galactic evolution.

Critically, the models of this work can be broadly categorized as either having bursty or smooth stellar feedback. FIRE, SPICE Bursty, and Thesan Zoom have bursty stellar feedback, while SPICE Smooth and Thesan Box have smooth stellar feedback. In this Section, we introduce the simulation models (§2.1), detail our selection criteria (§2.2), and then define our method for obtaining the gas-phase metallicity gradients from each galaxy (§2.3).

2.1. Simulations

2.1.1. FIRE

The FIRE cosmological zoom-in simulations of galaxy formation analyzed here run using the multi-physics simulation code GIZMO (Hopkins 2015) and the meshless finite mass scheme for hydrodynamics (ref). The FIRE-2 physics model we employ here (Hopkins et al. 2018) builds upon and improves the original FIRE-1 model (Hopkins et al. 2014).

Star formation in the FIRE model occurs in dense, self-gravitating, Jeans-unstable molecular gas with $n_{\rm H} > 1000$ cm^{-3}. The requirement of locally self-gravitating gas leads to star formation at an efficiency of 100% per free fall time; however, the star formation is regulated by feedback processes. Newly formed star particles inherit their mass and metallicity from the gas in which they formed. The stellar evolution models in FIRE come from STARBURST-99 v7.0 (Leitherer et al. 1999, 2014) assuming a Kroupa (2002) IMF with masses in the range $0.1 - 100$M$_\odot$. Feedback from stars is implemented through four different channels: (i) radiation pressure, (ii) supernovae with rates set by STARBURST-99 for Type II and Mannucci et al. (2006) for Type Ia, (iii) stellar winds from OB and AGB stars with rates set by STARBURST-99, and (iv) photo-electric heating. The feedback events return mass and metals to the ISM as well as drive galactic winds and outflows. The FIRE model explicitly tracks the evolution of 11 chemical species (H, He, C, N, O, Ne, Mg, Si, S, Ca, and Fe). The yields of these species from stellar feedback events come from van den Hoek & Groenewegen (1997), Marigo (2001), and Izzard et al. (2004) for stellar winds, Nomoto et al. (2006) for core-collapse supernovae, and Iwamoto et al. (1999) for Type Ia supernovae. All of the FIRE simulations analyzed in this work implement an explicit model for unresolved turbulent metal diffusion (Hopkins 2017; Su et al. 2017; Escala et al. 2018).

We use data products from the FIRE-2 public data release (Wetzel et al. 2023, 2025), for which several galaxies were made public as part of the "core" and "high-redshift" samples (for the complete details on each sample we refer the reader to Wetzel et al. 2023, 2025). Our main investigation of the FIRE model in this work focuses on the high-redshift sample: 22 galaxies run down to $z = 5$ (z5m09a,b, z5m10a,b,c,d,e,f, z5m11a,b,c,d,e,f,g,h,i, and z5m12a,b,c,d,e), 6 galaxies run down to $z = 7$ (z7m11a,b,c and z7m12a,b,c), and 6 galaxies run down to $z = 9$ (z9m11a,b,c,d,e and z9m12a). However, for Section 4.1 we also employ data products from 14 galaxies from the core base sample (m09, m10q,v, m11b,d,e,h,i,q, m12b,c,f,i,m,r,vw,z). The simulations within both of these samples come from: Wetzel et al. (2016), Garrison-Kimmel et al. (2017), Chan et al. (2018), El-Badry et al. (2018), Hopkins et al. (2018), Ma et al. (2018), Garrison-Kimmel et al. (2019), Ma et al. (2019), Ma et al. (2020), and Samuel et al. (2020). The name of the simulation corresponds to the approximate halo mass at the final snapshot ($z = 0$ for the core sample and $z = 5, 7, 9$ for the high redshift samples). The simulations were run at a number of different baryon mass resolutions, ranging from ~ 100 M$_\odot$ for the smaller halos to ~ 7000 M$_\odot$ for larger halos. We refer the reader to Wetzel et al. 2023 and the works listed above for more details on each simulation model. Finally, we note that the FIRE-2 simulations we use here do not include AGN feedback, magnetic fields, or cosmic rays.

For the analysis of FIRE, we use both the GIZMO ANALYSIS and HALO ANALYSIS tools provided by Wetzel et al. (2016).

2.1.2. SPICE

We also use data products from the SPICE cosmological simulations (Bhagwat et al. 2024). SPICE is a series of cosmological box simulations run with the RAMSES-
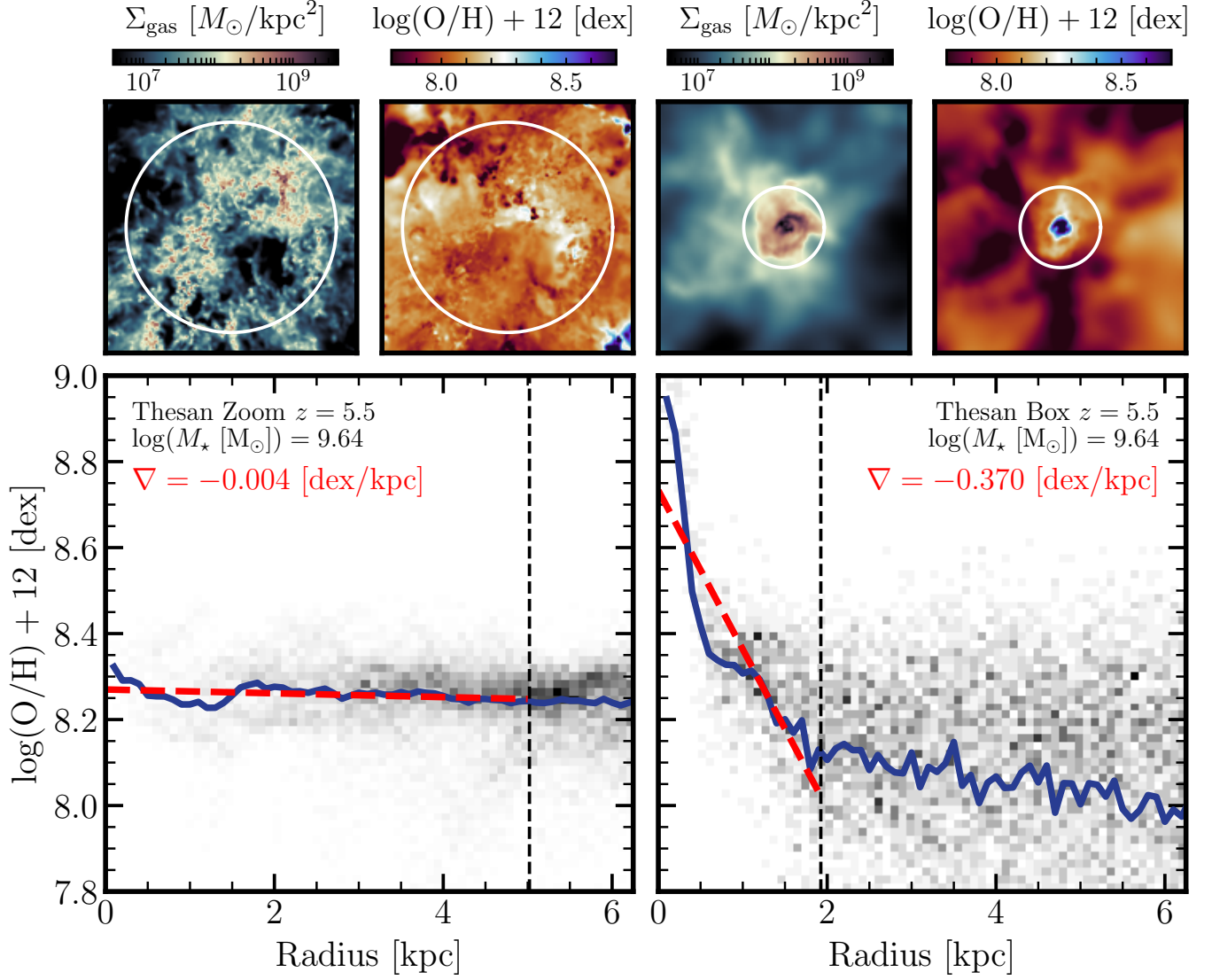
Figure 2. Example Bursty and Smooth Feedback Gradients. The gas mass surface density (top row, first and third panels) and gas-phase metallicity maps (top row second and fourth panels) within 6 kpc for a galaxy with stellar mass $10^{9.64}$ M$_\odot$ at $z = 5.5$ in Thesan Zoom (left panels) and Thesan Box (right panels) simulations. The radial distribution of metals is shown with a 2D histogram in the background of the bottom two panels. The solid blue line represents the median metallicity profile in bins of 0.1 kpc. The dashed red line shows a linear regression through the median profile at radii smaller than $R_{\rm out}$ (the radius enclosing 90% of all star formation in the galaxy). The slope of the dashed line is our reported metallicity gradient. We quote the gradient for both galaxies in the bottom panels, finding that the Thesan Zoom galaxy has a significantly flatter gradient than that of Thesan Box.

RT code (Rosdahl et al. 2013; Rosdahl & Teyssier 2015), which is an extension of the original RAMSES adaptive mesh refinement code (Teyssier 2002). The main advantages of the SPICE simulations is their variations in the treatment of stellar feedback. SPICE implements two different feedback models: smooth-sn and bursty-sn (hereafter "SPICE Smooth" and "SPICE bursty", respectively). The SPICE Smooth model allows for stars within the particles to explode anywhere from 3-40 Myr after birth (depending on their mass and rates set by

STARBURST-99), leading to smoother injection of energy back into the ISM. The SPICE Bursty model, on the other hand, assumes that all supernovae go off in a single event 10 Myr after birth. Populations of stars exploding concurrently makes stellar feedback particularly efficient in the SPICE Bursty model. It should be noted that the SPICE approach of modifying delay time distributions of supernovae is different than the bursty feedback in FIRE and Thesan Zoom. However, the key advantage of SPICE for the purposes of this work is the

same physical model with different feedback implementations.

Stars form in the SPICE model according to prescriptions set in Kretschmer & Teyssier (2020) which incorporate a model for (unresolved) turbulence (Schmidt et al. 2006) allowing for variable star formation rate efficiencies that depend on the local conditions of the ISM (i.e., the virial parameter and turbulent mach number; Hennebelle & Chabrier 2011, Federrath & Klessen 2012). Star formation in SPICE therefore occurs in two modes: in gravitationally unstable gas and regions with large amounts of supersonic turbulence. This star formation occurs in dense ($n_{\rm H} \geq 10$ cm^{-3}) gas and forms stars according to a Chabrier (2003) IMF. Feedback from these stars comes in the form of radiative energy (photo-ionization and -heating) in addition to the aforementioned supernova feedback variations. Metals are advected across cell boundaries as passive scalars (following from Rosdahl et al. 2013). Finally, we note that SPICE does not implement feedback from black holes. Each of the SPICE boxes we analyze here have a volume of $(10$ cMpc$/h)^3$ at initial baryon mass resolution of 975M$_\odot$.

2.1.3. Thesan

Finally, we use data products from the Thesan suite of simulations. Thesan consists of a large $(95.5$ cMpc$)^3$ box (Garaldi et al. 2022; Kannan et al. 2022; Smith et al. 2022, hereafter Thesan Box), as well as a series of high resolution zoom-in simulations (Kannan et al. 2025, hereafter Thesan Zoom). Both the box and zooms are run using the radiation hydrodynamics moving-mesh code AREPO-RT (Kannan et al. 2019; based on the original AREPO code Springel 2010). Both Thesan Box and Thesan Zoom add an additional model for the creation and destruction of dust from gas according to McKinnon et al. (2016, 2017). While the details of the dust module are beyond the scope of this work, it is important to note that the dust forms out of the metals in the gas phase. Therefore, some component of the metals are lost to dust formation. Moreover, both Thesan Box and Thesan Zoom explicitly tracks the evolution of several chemical species (H, He, C, N, O, Ne, Mg, Si, and Fe) with yields coming from Nomoto et al. (1997) for Type Ia supernovae, Portinari et al. (1998) and Kobayashi et al. (2006) for Type II supernovae, Karakas (2010), Doherty et al. (2014), and Fishlock et al. (2014) for AGB winds.

Thesan box is run using a modified version of the IllustrisTNG galaxy formation model (Pillepich et al. 2018), which incorporates the physics of both stellar and AGN feedback. Stars form in the dense ($n_{\rm H} \gtrsim 0.1$ cm^{-3}) ISM

according to the Springel & Hernquist (2003) equation of state and a Chabrier (2003) IMF. The Springel & Hernquist (2003) equation of state provides pressure support for the ISM and sets the efficiency at which stars form from the dense gas. Feedback from these stars is implemented in the form of supernovae explosions and stellar winds in the form of kinetic and thermal energy (see Pillepich et al. 2018). Black holes with mass $\sim 10^6$ M$_\odot$ are seeded in halos exceeding 7×10^{10} M$_\odot$ in the Thesan Box model. Feedback from black holes is modeled via two channels based on the accretion rates of the black holes: the high accretion thermal mode and low accretion kinetic mode (see Weinberger et al. 2018). The thermal mode continuously dumps thermal energy into the ISM and dominates for low mass systems, whereas high mass galaxies are dominated by the directed and pulsed kinetic winds. We utilize the highest resolution Thesan-1 volume which is a $(95.5$ cMpc$)^3$ box with 2×2100^3 particles, corresponding to an initial baryon mass resolution of 3.12×10^6 M$_\odot$.

Thesan Zoom employs a tailored version of the SMUGGLE galaxy formation model (Marinacci et al. 2019), which shares a number of similarities with FIRE. Stars form in dense ($n_{\rm H} > 10$ cm^{-3}), self-gravitating, Jeans-unstable gas with an efficiency per free-fall time of 100%. Similar to FIRE, the global star formation is self-regulated by feedback from the newly formed stars and maintains a lower efficiency compared to the prescribed local value (Shen et al. 2025; Wang et al. 2025). Stellar feedback in Thesan Zoom is modeled through a number of different channels: radiative feedback (Kannan et al. 2020), stellar winds and supernovae (Marinacci et al. 2019), and "early" stellar feedback (i.e., momentum feedback in the first 5 Myr of star particles life time; Kannan et al. 2025). Notably, the Thesan Zoom suite includes several variations in these feedback prescriptions; however, for this work, we use only the fiducial model. We note that Thesan Zoom does not include contributions from AGN. The Thesan Zoom Suite consists of 14 halos run down to $z \sim 3$ at various baryon mass resolutions ranging from 142 M$_\odot$ to 9.09×10^3 M$_\odot$ (see Kannan et al. 2025 their Table 2). We make use of the highest resolution versions of each halo available (see Kannan et al. 2025 their Table 3).

2.2. Galaxy Selection Criteria

The three simulation models of this work adopt the following halo finding algorithms: SPICE uses AdaptaHOP , FIRE adopts Amiga Halo Finder (Knollmann & Knebe 2009), and Thesan employs Subfind (Springel et al. 2001). While the structure finding algorithms are not the same and can thus assign different particles/cells

to the various (sub)structures (e.g., Forouhar Moreno et al. 2025), we do not anticipate the detailed properties of the very inner regions of galaxies (∼few kpc) to be significantly impacted by the different structure finders.

The simulations also have different resolutions, even within the same galaxy formation model (e.g., Thesan Zoom and FIRE). To ensure that our galaxies are well-resolved, we require a threshold of $> 10^3$ gas and star particles within the system (following from Garcia et al. 2025b). Roughly speaking, this corresponds to minimum stellar and gas masses of $\sim 10^6$ M$_\odot$ in SPICE as well as high resolution FIRE and Thesan Zoom runs, $\sim 10^7$ M$_\odot$ in lower resolution FIRE and Thesan Zoom runs, and $\sim 10^8$ M$_\odot$ in the Thesan Box. Moreover, since emission line metallicity diagnostics come from star-forming HII regions (e.g., Kewley et al. 2019), we require that our galaxies have instantaneous non-zero star formation rates. Finally, we note that we restrict our analysis to the most massive subhalo within each group (i.e., the central galaxy).

2.3. Gradient Definition

We largely follow the methodology of Garcia et al. (2025b; which itself derives heavily from a combination of Ma et al. 2017 and Hemler et al. 2021) to define the metallicity gradients with only a few minor changes. We first briefly describe the methodology employed in this work, then note any changes from the previous methodology, and briefly discuss how they may impact our results. We demonstrate the application of these methodologies on two galaxies in Figure 2.

We first center the galaxy and rotate it to the face-on orientation. To rotate the galaxy to face-on, we define the angular momentum vector of star-forming gas within a region $R_{in} < r < R_{out}$ (where R_{in} and R_{out} are the regions containing 5% and 90% of the total star formation of the galaxy, respectively). We then align this angular momentum vector along the $+z$ axis. We note that the concept of "face-on" for galaxies with bursty feedback is not as well posed as for the more disk-like galaxies of smooth feedback models (see, e.g., Figure 2). To make as fair a comparison as possible, we re-orient all galaxies in each model according to the above prescription. Since the ISM of bursty feedback galaxies lacks coherent structure, we do not anticipate that the (re-)orientation plays a significant role in our results.

With our face-on galaxy, we create two-dimensional mass-weighted metallicity maps and gas mass maps using pixel sizes of 0.1 kpc × 0.1 kpc (shown in the top row of Figure 2). We then convert the two-dimensional maps into one-dimensional radial distributions (gray background distribution in large panels of Figure 2).

We further reduce the radial distribution of metals into a singular median metallicity profile in bins of 0.1 kpc (solid blue lines in large panels of Figure 2). We note that, since metallicity emission line diagnostics come from star-forming regions in galaxies, we restrict our sample to pixels with gas mass surface densities $> 10^6$ M$_\odot$ kpc^{-2} (which are likely to host star-forming gas; Ma et al. 2017). Finally, we summarize the median metallicity profile by fitting a linear regression (in logarithmic metallicity) in the region $r < R_{out}$ (dashed red lines in Figure 2). We note that a single linear regression is a simplistic summary statistic for metallicity profiles (see, e.g., bottom right panel of Figure 2). Many of the profiles flatten out at large radii (see also Garcia et al. 2023) and/or may have multiple components (see also Tapia-Contreras et al. 2025); however, a detailed examination of the shapes of the profiles of these simulations is beyond the scope of the current work.

The largest difference between the methodology applied in this work and that of Garcia et al. (2025b) is that here we do not truncate the gradient measurement at an inner radius. The reasoning behind ignoring the central regions of galaxies in the previous work was primarily to eliminate the impact of AGN, which can significantly suppress metals in the inner regions and contaminate emission line diagnostics. This practice is commonly adopted in low redshift studies (e.g., Sánchez et al. 2012, 2014; Sánchez-Menguiano et al. 2016; Belfiore et al. 2017). At higher redshift, however, it is less common to exclude the inner regions (e.g., Vallini et al. 2024; Venturi et al. 2024; Fujimoto et al. 2025) and most of the simulations here do not model AGN (although Thesan Box does).[2] We therefore relax the inner region criterion for this work, noting its inclusion (or lack thereof) does not significantly impact our core results. Finally, we note that SPICE does not trace the evolution of individual metal species. The gradients we quote in SPICE are therefore the *total* metallicity gradient scaled by assuming at 35% fraction of Oxygen in metals and a total mass fraction that is 76% Hydrogen – opposed to the direct Oxygen-to-Hydrogen abundances of the other models. In practice, there is generally only a modest ($\lesssim 0.1$ dex) difference between the the scaled total metallicity and direct Oxygen-to-Hydrogen

---

[2] While Thesan Box does model AGN feedback, we do not expect that it will have a significant impact on the galaxies in our sample. As mentioned in Section 2.1.3, the kinetic mode AGN feedback (which is the mode most dominant in quenching galaxies and driving the interior metallicity variations; Weinberger et al. 2017) effectively only impacts massive galaxies, thus the impact of AGN should be minimal in our sample.

abundances (see Garcia et al. 2025a, Appendix B and Figure B2).

3. RESULTS

3.1. *Distribution of Metallicity Gradients in each simulation*

We begin by characterizing the metallicity gradients in each simulation. Figure 3 shows the probability density function (PDF) of all of the measured gradients in the bursty feedback models (top left is Thesan Zoom, top middle is SPICE Bursty, and top right is FIRE) and the smooth feedback models (bottom right is Thesan Box on bottom middle is SPICE Smooth). We note that combining the gradients in this way is a crude comparison, since it ignores several important factors, e.g., the redshift of the galaxy or its stellar mass (both of which we explore in more detail in Section 3.2). Despite the crudeness of the comparison, we find a qualitative difference in the gradients measured in the smooth feedback models to those of the bursty feedback models, with the latter typically having flatter gradients.

To quantify the discrepancy between the two different types of simulations, the bottom right panel of Figure 3 shows the median and spread (taken to be the 16th and 84th percentiles of the distributions) for each model analysed in this work. We find that the median gradients are $-0.021^{0.008}_{-0.072}$ dex/kpc in Thesan Zoom, $-0.133^{0.038}_{-0.334}$ dex/kpc in SPICE Bursty, $-0.020^{0.021}_{-0.074}$ dex/kpc in FIRE, $-0.205^{-0.124}_{-0.373}$ dex/kpc in Thesan Box, and $-0.265^{-0.553}_{-0.066}$ dex/kpc in SPICE Smooth. On the whole, the bursty feedback models are significantly flatter than their smooth counterparts. For the Thesan simulations, the gradients in the Box are approximately an order of magnitude steeper than their Zoom counterparts, while the SPICE Smooth gradients are steeper than the SPICE Bursty by a factor of ~ 2. Moreover, the width of the distribution of gradients in the bursty models is significantly smaller than those of the smooth models, with the exception of SPICE which have comparable scatter. In each of the samples, we find that the distributions tend to be skewed towards more negative gradients, with the 16th percentiles being further from the median than the 84th percentiles. Clearly, even without more careful considerations for the detailed properties of the individual systems, there is a qualitative difference between the metallicity gradients from bursty and smooth feedback models.

It is also worth noting how remarkable the ubiquity of the gradients between the similar models is, regardless of detailed simulation implementation. This similarity echoes the low redshift, large box simulations we investigated previously (Garcia et al. 2025b). While each

simulation model – both in this work and in Garcia et al. (2025b) – is attempting to model the same general physics (e.g., star formation, stellar feedback, chemical enrichment), there is a wide diversity of numerical implementations and assumptions that go into the different models (see, e.g., Section 2.1). Yet, despite these differences, the metallicity gradients in each of the models have highly self-similar trends: smooth feedback models have strong negative gradients while bursty feedback models have flatter gradients. There is, of course, variation between the predictions when considering properties of the host galaxies (which we discuss more in the next section); however, the level of out-of-the-box agreement is worth appreciating. This agreement is especially remarkable given that the total metal budget of galaxies in different simulation models can vary substantially (Garcia et al. 2024b, 2025a). Thus, we emphasize the utility of metallicity gradients as a diagnostic for stellar feedback at high redshift ($z \gtrsim 3$), which we discuss in more detail in Section 4.1.

3.2. *Gradients as a Function of Stellar Mass and Redshift*

We now more carefully consider our sample of galaxies. The main properties that we investigate here are: (i) the stellar mass of the host galaxy, and (ii) the redshift of the galaxy. Figure 4 shows the metallicity gradients of galaxies in each of the simulation models as a function of redshift, broken into four different stellar mass bins corresponding to galaxies in that mass bin at the given redshift (i.e., not explicitly tracking progenitors through time). We only plot values at integer and half-integer redshifts (e.g., $z = 5.0$ and $z = 5.5$) for clarity, but data from Thesan Box, Thesan Zoom, and FIRE includes gradients measured at intermediate redshifts (e.g., $z = 5.2$). Finally, we also note that we require more than five galaxies in each bin to plot it.

The gradients in SPICE Smooth model in the lowest mass bin ($M_\star < 10^8$ M$_\odot$; top left of Figure 4) have virtually no dependence on redshift, with an average value of ~ -0.2 to -0.3 dex/kpc. The spread in gradients in this stellar mass bin for SPICE Smooth is significant, covering ± 0.3 dex/kpc. The galaxies in SPICE Smooth therefore cover a wide diversity of positive, negative, and flat gradients in this mass bin. The bursty feedback models – FIRE, SPICE Bursty, and Thesan Zoom – also have very little redshift evolution in this mass bin and have flatter gradients on average than SPICE Smooth. The scatter about these gradients is less than SPICE Smooth, covering approximately ± 0.1 dex/kpc in FIRE and Thesan Box, whereas the scatter in SPICE Bursty is comparable to SPICE Smooth. On the whole,
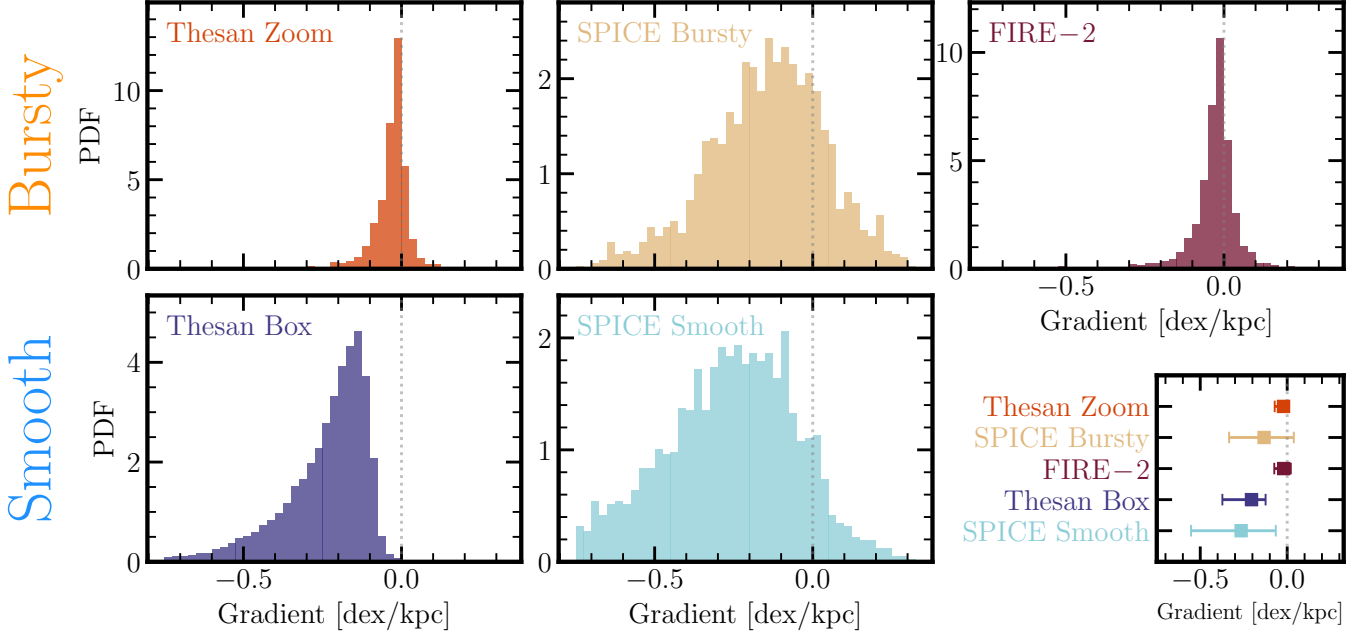
Figure 3. Distribution of Gas-Phase Radial Metallicity Gradients in Bursty and Smooth Feedback Models at High Redshift ($3 < z \lesssim 11$). Our sample of metallicity gradients in Thesan Zoom (top left), SPICE Bursty (top middle), FIRE-2 (top right), Thesan Box (bottom left), and SPICE Smooth (bottom middle). The top row represent the bursty feedback models, while the bottom row represents the smooth feedback models. We summarize the distributions in the small figure in the bottom right with the median, 16th percentile, and 84th percentile of the distributions. We find that the gradients in the smooth feedback models are systematically more negative than their bursty feedback counterparts.

we find that there are no significant differences between the metallicity gradients of smooth and bursty feedback models in this lowest mass bin.

In the next mass bin (10^8 M$_\odot$ < $M_\star$ < 10^9 M$_\odot$; top right of Figure 4), the smooth feedback models have qualitatively similar average gradients as the lowest mass bin: around -0.2 to -0.3 dex/kpc with little redshift evolution. The distribution of gradients (± 0.1 dex/kpc), though, is much smaller than in the previous mass bin at $z \gtrsim 7$, but is comparable to the previous mass bin at $z = 5 - 6$. This suggests that the gradients in these lower mass galaxies are far more subject to variation. In the bursty feedback models, we also find qualitatively similar behavior as the lowest mass bin: flat gradients with very little redshift evolution. The full distribution of gradients in the bursty feedback models is approximately the same as the lowest mass bin $\sim \pm 0.1$ dex/kpc. In this mass bin, there is more of a difference between the smooth and bursty models, but the difference is subtle.

The difference between the smooth and bursty models is more apparent in the next highest mass bin, though (10^9 M$_\odot$ < $M_\star$ < 10^{10} M$_\odot$; bottom left of Figure 4). The smooth feedback models still have virtually no redshift evolution in this mass bin and their average gradients are of the order of -0.3 dex/kpc, but the distri-

bution of gradients increases. Specifically, there exist many more very strong ~ -0.5 dex/kpc gradients with a "ceiling" of approximately -0.15 dex/kpc. The distribution of gradients changes for the bursty feedback models, too. The width of the distribution shrinks to ~ 0.05 dex/kpc. Here, the qualitative difference between the smooth and bursty feedback models becomes more apparent. There are very few flat gradients in the smooth feedback models in this stellar mass range (only $\sim 2\%$ of galaxies have gradients shallower than -0.075 dex/kpc) and there are virtually no strong negative gradients in the bursty feedback models (only $\sim 3\%$ of galaxies have gradients steeper than -0.075 dex/kpc).

Finally, the difference between the smooth and bursty feedback models is most clear in the highest mass bin ($M_\star > 10^{10}$ M$_\odot$; bottom right of Figure 4). At this stellar mass there are only a few galaxies from the bursty sample (see, e.g., Bhagwat et al. 2024 that bursty feedback models produce galaxies with lower stellar mass at fixed halo mass). Regardless, the few galaxies in FIRE and Thesan Zoom still have very flat gradients with very little scatter. For the smooth feedback models, we find a strong relationship between gradient and redshift in this most massive bin. Galaxies in Thesan Box have (already quite strong) gradients of ~ -0.4 dex/kpc at $z = 5-5.5$, which increases to average gradients of ~ -0.8 dex/kpc
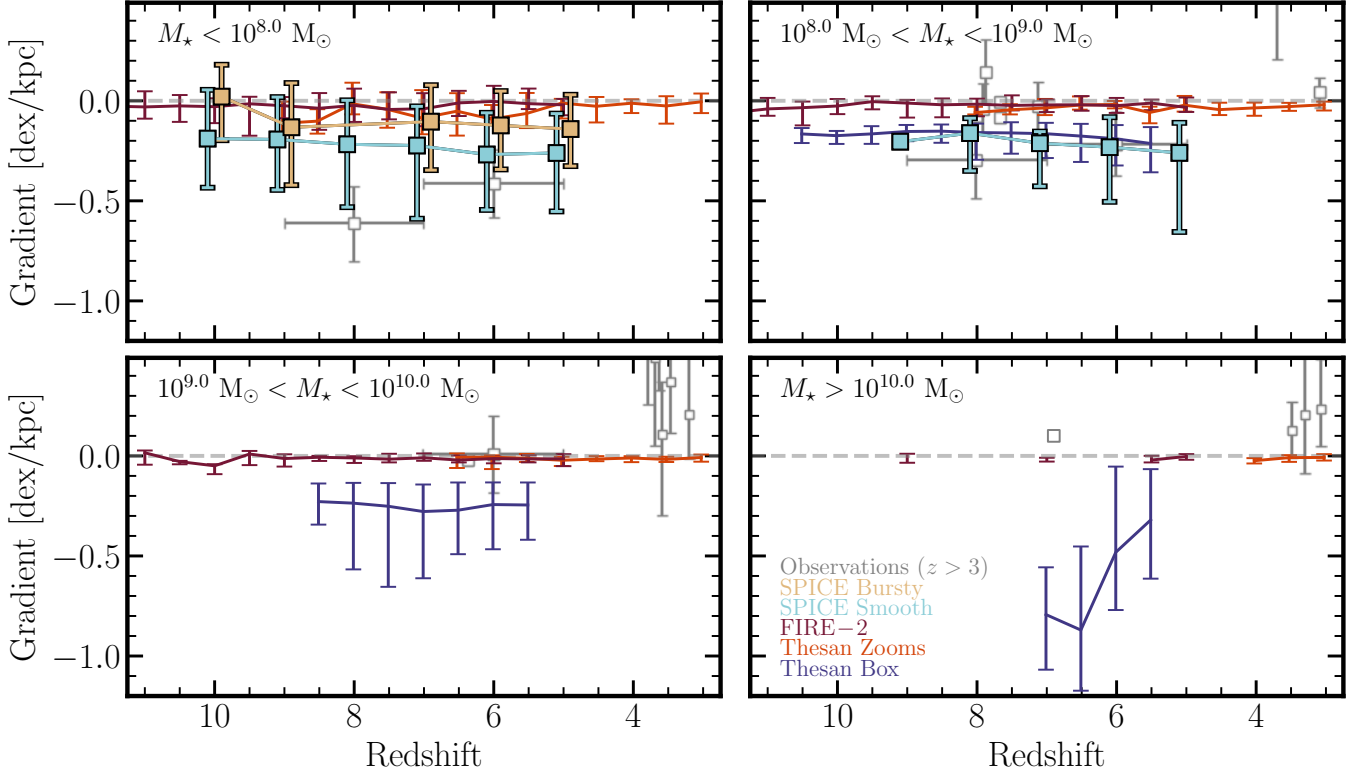
Figure 4. Metallicity Gradient Evolution Broken into Four Stellar Mass Bins. The gradient evolution in FIRE-2 (triangles), SPICE (squares), and Thesan (solid lines) broken into stellar mass bins: $M_\star < 10^{8.0}$ $M_\odot$ (top left), $10^{8.0}$ $M_\odot < M_\star < 10^{9.0}$ $M_\odot$ (top right), $10^{9.0}$ $M_\odot < M_\star < 10^{10.0}$ $M_\odot$ (bottom left), and $M_\star > 10^{10.0}$ $M_\odot$ (bottom right). We also include a recent series of observed metallicity gradients from *JWST* (when stellar mass estimates available; Troncoso et al. 2014; Arribas et al. 2024; Venturi et al. 2024; Acharyya et al. 2025; Ivey et al. 2025; Li et al. 2025).

at $z = 7$. At $z = 7$, there is a delineation of approximately an order of magnitude in the metallicity gradients of the galaxies. We investigate this in more detail, and compare with the one observed galaxy at this redshift, in Section 4.2.

In all, we find that the level to which the metallicity gradients of galaxies in smooth and bursty feedback models disagree depends on stellar mass. We find that the gradients in galaxies with the largest stellar masses ($M_\star \gtrsim 10^9$ $M_\odot$) are the most discordant between the different models. Low mass galaxies ($M_\star \lesssim 10^9$ $M_\odot$), on the other hand, are only quantitatively different, not qualitatively, with the very low mass galaxies ($M_\star < 10^8$ $M_\odot$) being largely indistinguishable between the different feedback types.

4. DISCUSSION

4.1. *13 Billion Years of Gradient Evolution from Cosmological Simulations*

Figure 5 shows the redshift evolution of metallicity gradients in nine modern cosmological simulation models. We categorize each simulation model as having either bursty or smooth stellar feedback. The bursty

feedback models are FIRE-2 (Hopkins et al. 2018), Thesan Zoom (Kannan et al. 2025), and SPICE Bursty (Bhagwat et al. 2024), while the smooth feedback models are EAGLE (Schaye et al. 2015), Illustris (Vogelsberger et al. 2014), IllustrisTNG (Pillepich et al. 2018), SIMBA (Davé et al. 2019), Thesan Box (Kannan et al. 2022), and SPICE Smooth (Bhagwat et al. 2024). The data from the EAGLE, Illustris, TNG, and SIMBA simulations direclty comes from Garcia et al. (2025b; see caveat about slight change in methodology in Section 2.3). We note that this plot also includes FIRE-2 galaxies from the "core" sample. We treat these systems the same as their high redshift counterparts and only report gradients at integer and half-integer redshifts at $z < 5$. Briefly, we find that our analysis of the FIRE-2 core sample at $z < 5$ is consistent with previous FIRE papers, finding a diversity of metallicity gradients with a preference for flat gradients (Ma et al. 2017; Bellardini et al. 2021; Graf et al. 2024; Sun et al. 2024).

Figure 5 is essentially an updated version of Gibson et al. (their Figure 1), which included the evolution of four galaxies to $z \sim 2.5$. Gibson et al. (2013) find that the systems with 'enhanced' feedback have flat gradi-
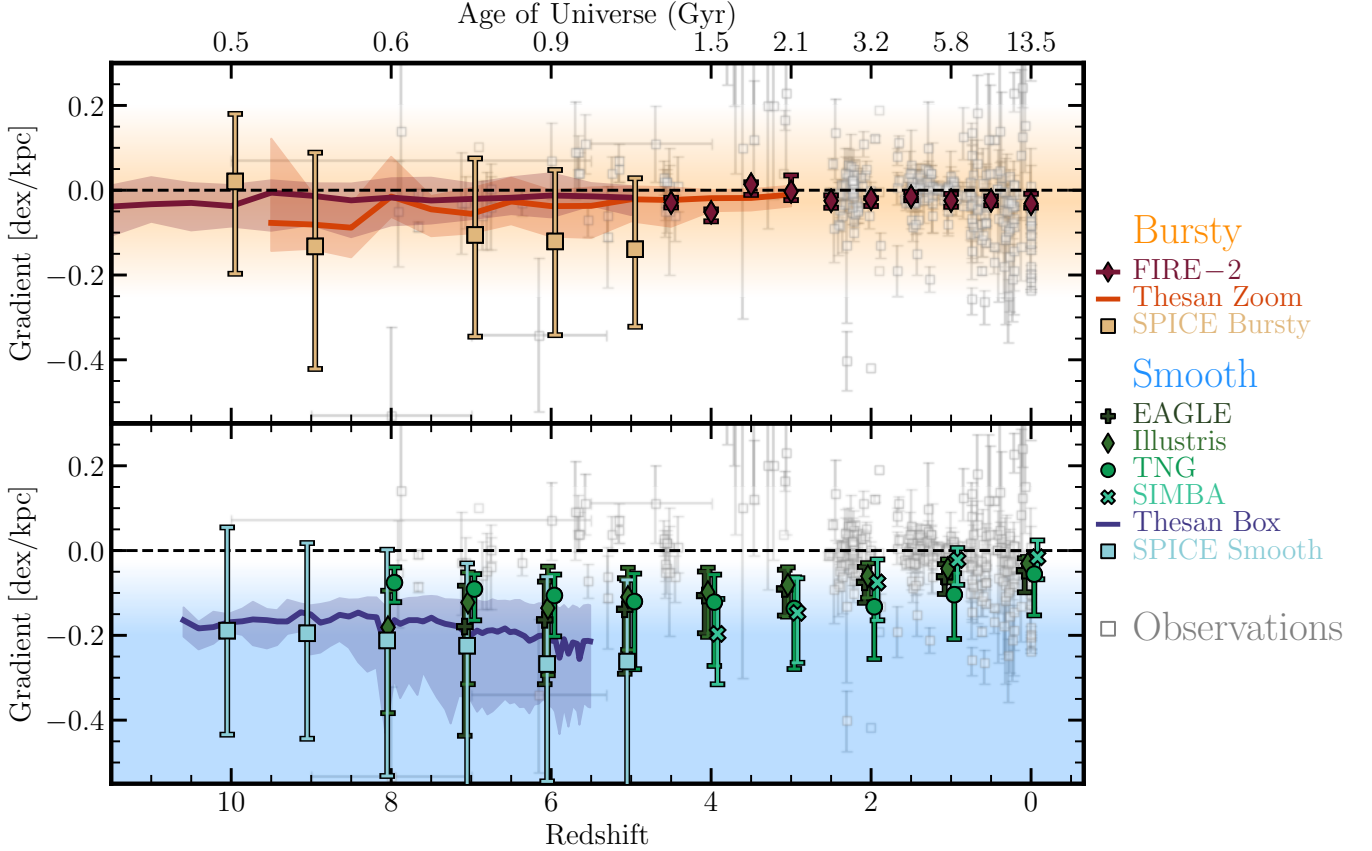
Figure 5. 13 Billion Years of Gas-Phase Metallicity Gradient Evolution in Cosmological Simulations. The composite evolution of metallicity gradients from this work and Garcia et al. (2025b) in (**Top**) bursty feedback models FIRE-2 (maroon diamonds), Thesan Zoom (solid orange line), and SPICE Bursty (orange squares), as well as (**Bottom**) smooth feedback models EAGLE (plus), Illustris (green diamonds), TNG (circles), SIMBA (Xs), Thesan Box (solid blue line), and SPICE Smooth (blue squares). In general, we find that bursty feedback models tend to have flatter metallicity gradients than their smooth feedback model companions, regardless of the detailed implementation of the models. The shaded regions in each panel *qualitatively* show where the majority of each feedback type's gradients lie, particularly at high redshift. We also present a compilation of observed metallicity gradients from Rupke et al. (2010b); Queyrel et al. (2012); Swinbank et al. (2012); Jones et al. (2013, 2015); Troncoso et al. (2014); Leethochawalit et al. (2016); Wang et al. (2017, 2019, 2022); Carton et al. (2018); Förster Schreiber et al. (2018); Curti et al. (2020); Grasha et al. (2022); Li et al. (2022, 2025); Arribas et al. (2024); Tripodi et al. (2024); Vallini et al. (2024); Venturi et al. (2024); Acharyya et al. (2025); Fujimoto et al. (2025); Ivey et al. (2025); Ju et al. (2025); Valé et al. (2025). Recent high redshift observations, with the exception of those from Li et al. (2025), seem to favor more bursty feedback scenarios.

ents, while systems with 'conservative' feedback have strong negative gradients that get stronger further back in time. Remarkably, we find qualitatively the same trend with the benefit of several additional simulation models and several orders of magnitude more galaxies. Galaxies with bursty feedback tend to have weaker metallicity gradients than their smooth feedback counterparts, especially at high redshift ($z \gtrsim 2$) and with large stellar masses (Figure 4 and Garcia et al. 2025b, Figure 3). The rate at which we find gradients to steepen with redshift in the smooth feedback models is approximately -0.02 dex/kpc/Δz (in good agreement with the values of Hemler et al. 2021; Garcia et al. 2025b), while

the bursty feedback models are roughly consistent with 0.00 dex/kpc/Δz.

We note that the strength of gradients appears to "taper" at the highest redshifts ($z \gtrsim 8$) in the smooth feedback models, instead of continuing the trend of stronger gradients with increasing redshift. We argue that this is likely a selection effect of the stellar masses within the samples at each redshift. As shown in Figure 4 (and Figure 3 of Garcia et al. 2025b), lower mass galaxies ($M_\star \lesssim 10^9$ $M_\odot$) in smooth feedback models tend to have flatter gradients than their high-mass counterparts (although it is unclear if this holds for galaxies at all redshifts for very massive $M_\star > 10^{11}$ $M_\odot$ galaxies; see

Garcia et al. 2025b). The sample of galaxies in, e.g., Thesan Box and SPICE Smooth tends towards lower mass systems at these very early times. We therefore suggest that, given a mass complete sample, it is likely that the gradients would continue to steepen at redshifts $z > 8$ and that the observed tapering is just a selection effect from the cosmological volumes.

4.2. Comparison with High Redshift ($z > 3$) Observations

We now make a detailed comparisons to observed gas-phase metallicity gradients, with an emphasis on high redshift ($z > 3$). We provide a more detailed comparison with low redshift observations in the smooth feedback models in Section 4.3.1 of Garcia et al. (2025b). We note that the FIRE-2 core sample also spans $z < 5$, which we did not discuss previously. Briefly, we find the lower redshift FIRE-2 sample to be broadly consistent with the wide diversity of gradients observed at low redshift (see also Ma et al. 2017; Sun et al. 2024, for more detailed comparisons of metallicity gradients at $z < 5$ in FIRE-2 galaxies).

There have been several observations of metallicity gradients at redshifts $z > 3$ to date (Troncoso et al. 2014; Arribas et al. 2024; Tripodi et al. 2024; Vallini et al. 2024; Venturi et al. 2024; Rodríguez Del Pino et al. 2024; Acharyya et al. 2025; Fujimoto et al. 2025; Ivey et al. 2025; Li et al. 2025), with the majority coming from *JWST* in the last few years. We show these observational metallicity gradients in both Figure 4 and Figure 5 (noting that Figure 5 also contains observational gradients from $z < 3$). We note that stellar mass bins do not fit so neatly into our classification in Figure 4 for Li et al. (2025). We suspect, however, that the minor overlap in stellar mass does not significantly influence our comparison. On the whole, the current consensus at high redshift shows a preference for flatter metallicity gradients (which can be generally seen in Figure 3); however, stacked observations from Li et al. (2025) find very strong negative gradients. This picture seems to qualitatively align with the bursty feedback models presented in this work (although it does not necessarily suggest that feedback in the observed Universe is necessarily as bursty as these simulations; see discussion in Section 4.2.2).

We further consider the stellar mass of the observed galaxies, when available. In our lowest mass bin ($M_\star < 10^8$ M$_\odot$; top left of Figure 4), Li et al. (2025) have measured the gradients of stacked galaxies from $z \sim 5 - 9$ finding strong negative gradients. These strong gradients are most consistent with the SPICE Smooth simulations; however, as noted in Section 3.2, this mass range

is not very discriminatory between the different feedback models. As mentioned in Section 3.2, the bursty feedback models have a wider spread of gradients in this stellar mass bin. Therefore, while the stacked gradients from Li et al. (2025) are potentially suggestive of smooth feedback scenarios, the larger spread in bursty feedback models complicates the picture. Observational gradients in the mass bin 10^8 M$_\odot < M_\star < 10^9$ M$_\odot$ (top right panel of Figure 4) are mostly consistent with no gradient (Venturi et al. 2024; Ivey et al. 2025; Acharyya et al. 2025), with the exceptions of the strong stacked gradients at $z \sim 5 - 9$ (Li et al. 2025) and a strongly inverted gradient at $z \sim 4$ (Troncoso et al. 2014). As with the lowest mass bin, the observed gradients here are also suggestive. The gradients from Venturi et al. (2024), Ivey et al. (2025), and Acharyya et al. (2025) are most similar to those of the bursty stellar feedback models; however, the gradients are only quantitatively different to smooth feedback models, not qualitatively different. In the mass bin 10^9 M$_\odot < M_\star < 10^{10}$ M$_\odot$ (bottom left panel of Figure 4) the few observed gradients (Troncoso et al. 2014; Venturi et al. 2024; Li et al. 2025) are more suggestive of bursty feedback (although the $z \sim 3 - 4$ inverted gradients are difficult to reconcile, see discussion in Section 4.2.3 below). The sample sizes at $z > 5$ are small, but both the stacked observations and measurement of an individual galaxy are highly consistent with the flat gradients from both FIRE and Thesan Zoom, compared to the strong negative gradients in Thesan Box.

In the highest mass bin ($M_\star > 10^{10}$ M$_\odot$), there is only one gradient quoted in the literature (Arribas et al. 2024) at $z > 5$ with a few from Troncoso et al. (2014) at $z \sim 3 - 4$ (which we discuss in more detail in the following subsection). Since there are only a few systems with this mass in both the observed and simulated samples at $z = 7$, Figure 6 shows the metallicity gradients of all analogs to the observed galaxy (SPT0311-58 E). Specifically, there are six objects at z=7 with the same stellar mass of to SPT0311-58 E at $z = 7$ in our simulation samples: three in the FIRE high redshift sample (z7m12a, b, and c) and three in Thesan Box (snapshot 55 subhalo ids 0, 433, and 1612).[3] In or-

---

[3] We note that these galaxies are selected as analogs to SPT0311-58 E purely based on their stellar mass and redshift. It is possible that these analogs may not be direct analogs in many important ways (e.g., environment, assembly history, etc). Moreover, there is some debate as to whether stellar masses can be derived robustly at these high redshifts (see, e.g., Narayanan et al. 2024b; Cochrane et al. 2025). We therefore caution against too strong an interpretation of the comparisons made between the observed sample and simulation analogs.
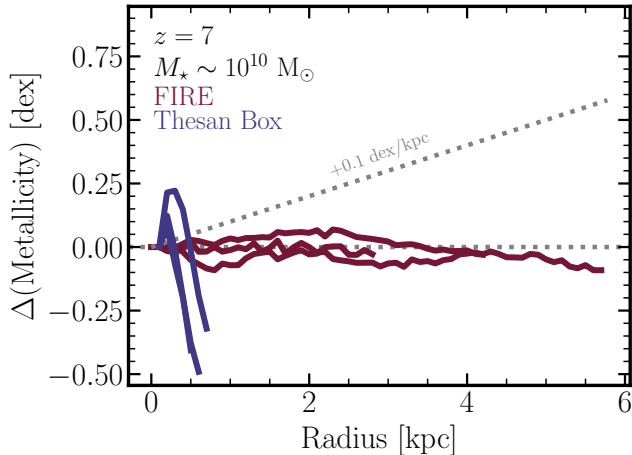
Figure 6. SPT0311-58 E Mass and Redshift Analogs in FIRE and Thesan Box. Comparison of metallicity profiles from $z = 7$ galaxies with stellar masses greater than 10^{10} M$_\odot$ (roughly corresponding to SPT0311-58 E Arribas et al. 2024) from FIRE (dark red lines) and Thesan Box (blue lines). The values on the ordinate are scaled to the central metallicity value of the profile for ease of comparison. As a reference, we also overplot a line corresponding to a +0.1 dex/kpc radial gradient, which is what Arribas et al. (2024) find the gradient of SPT0311-58 E to be. As we discuss in Section 4.2.3, simulation models generally struggle to reproduce strong positive gradients.

der to avoid normalization differences, we show the 1D median metallicity profiles in Figure 6 with respect to the central-most point of the profile. The extent of the profile corresponds to the extent of the region we take the gradient over (which, as demonstrated in Figure 2, can be thought of as a proxy for the size of the galaxy). We first note that the SPT0311-58 E analogs in Thesan Box are extremely compact, with most of their star formation taking place within the central ∼kpc of their centers (Shen et al. 2024b). The FIRE galaxies, on the other hand, are far larger, having the bulk of their star formation within $3 - 5$ kpc. The Thesan Box galaxies all have slightly off-center enhancement in metallicity by $\sim 0.1 - 0.2$ dex[4] followed by a sharp drop in the metallicity by $\sim 0.4 - 0.6$ dex. On the other hand, the FIRE galaxies show very little systematic variation in their median radial profiles. The measured gradients in Thesan are thus significantly steeper (~ -0.5 to -0.8 dex/kpc) than in FIRE (~ 0.0 dex/kpc). We note that none of the systems in FIRE or Thesan Box are particularly good

---

[4] The central enhancement may be caused by the kinetic mode AGN feedback in the Thesan Box model or, less physically, spatial softening lengths (which is ~ 0.2 physical kpc at this redshift, a significant fraction of the size of the galaxies) and/or small errors in the centering of the galaxy.

analogs to SPT0311-58 E in terms of a strong positive metallicity gradient, which we discuss further in Section 4.2.3. Regardless, we make a specific note of the *qualitatively* different nature of gradients in the smooth and bursty feedback models and suggest that further observations of massive galaxies at high redshift would prove highly informative for the nature of stellar feedback in the earliest epoch of galaxy formation.

4.2.1. *On Observational Systematics*

It should be noted that there are a number of observational systematics that may influence the measure of metallicity gradients of galaxies. The choice of metallicity calibration, for one, may have a significant impact on the measured gradient of observed galaxies. As a concrete example, Ivey et al. (2025) find that the measured gradient of their galaxy ID6355 goes from -0.008 ± 0.010 dex/kpc to -0.222 ± 0.041 dex/kpc with changes from strong line to direct electron temperature diagnostics, respectively.[5] Another important consideration is the impact of spatial resolution. As Yuan et al. (2013) show, the strength of metallicity gradients can be systematically flattened with angular lower resolution. In the smooth feedback models, the star-forming regions of galaxies at high redshift are highly compact (see Figure 6) with strong negative gradients. Outside of this region, the gradient flattens significantly (see Figure 2 for an example in Thesan Box). This gradient flattening is set by the competition between gas mixing and enrichment at large radii (Garcia et al. 2023). Observations of massive galaxies with poor spatial resolution could potentially wash out the small, high metallicity interiors of these galaxies and find a flatter gradient than we report here. The extent to which, e.g., the SPT0311-58 E analogs would be discriminatory for feedback physics in the early Universe is likely dependent on metallicity diagnostic and spatial resolution of the observations.

4.2.2. *On Simulation Modeling Limitations*

If the observations of flattened gradients are robust to the above systematics, there is evidence that the smooth feedback models may not sufficiently mix the metal content within their ISM. While rapid expulsions of gas driven by bursty stellar feedback is one method by which this mixing can be driven, it is not necessarily the only method. For example, diffusion of metals from unresolved turbulence within the ISM could play a significant role in redistributing metals and flattening gradients. Using the FIRE-2 model for this unresolved turbulence

---

[5] We note that in Figures 4 and 5 we quote the strong line diagnostic gradient from Ivey et al. (2025).

(described in Su et al. 2017; Escala et al. 2018; Hopkins et al. 2018), Bellardini et al. (2021) show that changes to the diffusion coefficients can systematically impact the radial distribution of metals. Specifically, those authors find that increased metal diffusion flattens metallicity gradients. It is therefore possible that the smooth feedback models require increased metal mixing from these unresolved eddies.

Increased turbulent diffusion mixes metals, but likely would not significantly change the overall total metal content. The existence – or lack thereof – of a correlation between the scatter about the mass-metallicity relation (MZR) and star formation rates (often referred to as the Fundamental Metallicity Relation; FMR) would therefore likely also be unimpeded in smooth feedback models with increased subgrid metal diffusion. While there is evidence that the FMR evolves in the smooth feedback models (i.e., the FMRs are weak and/or dynamic; Garcia et al. 2024b, 2025a), there still exists an anti-correlation between metallicity and SFR up to at least $z = 8$. Bursty feedback, on the other hand, should disrupt the interplay of gas accretion and metal return that gives rise to this anti-correlation (Garcia et al. 2024a,b, 2025a; Bassini et al. 2024; McClymont et al. 2025b). The existence of FMR-like anti-correlations between metallicity and SFR in the high redshift Universe – regardless of strong/weak or static/dynamic designation – could provide further constraining power as to whether flattened gradients are suggestive of bursty feedback or increased small-scale turbulent eddies within the ISM.

4.2.3. On the Dearth of Strong Positive Gradients in Simulations

There are three main ways proposed to create a strong positive (sometimes called inverted) metallicity gradient: (i) galaxy-galaxy mergers/interactions (e.g., Rupke et al. 2010a; Torrey et al. 2012; Grossi et al. 2020), (ii) pristine gas accretion onto the central regions of a galaxy (e.g., Cresci et al. 2010), and/or (iii) strong outflows (e.g., Rodríguez Del Pino et al. 2024). It is possible that the simulation sample preferentially omits merging systems at high redshift in the zoom-in simulations (FIRE and Thesan Zoom) since many of these targets were selected based on their relative isolation (Ma et al. 2018, 2019). However, it is not clear that this would be equivalently true for the full boxes (SPICE Smooth/Bursty, Thesan Box, EAGLE, Illustris, IllustrisTNG, and SIMBA). It is further unlikely that these samples preferentially select against galaxies that have gas accretion. We also know that the bursty feedback models do drive strong outflows of metals (Muratov et al. 2015, 2017). Yet, despite our models nominally including the impact of all three proposed mechanisms

required to invert gradients, there are very few galaxies in our entire sample (only $\sim 1.4\%$) that exhibit gradients greater than $+0.1$ dex/kpc, and are particularly rare at larger stellar masses and in smooth feedback models.

It is further interesting to note that Troncoso et al. (2014) present a whole population of strong positive metallicity gradients for ten galaxies at $M_\star > 10^9$ $M_\odot$ at $z \sim 3 - 4$. The gradients of these intermediate-to-high mass galaxies are difficult to explain with stellar feedback alone. Even our bursty feedback models do not have a significant population of high mass galaxies with inverted gradients. While there is some evidence that merging/interacting galaxies can produce strong positive metallicity gradients, Troncoso et al. (2014) suggest that the population of inverted gradients they observe at $z = 3 - 4$ are likely not mergers. Instead, Troncoso et al. (2014) suggest that the strong positive gradient could be caused by strong pristine gas accretion into the central regions of the galaxy.

Put more quantitatively, we overplot a dashed line of $+0.1$ dex/kpc on Figure 6, corresponding to the measured gradient of SPT0311-58 E (Arribas et al. 2024). While the Thesan Box and FIRE gradients have qualitatively different behavior (see discussion above), both models have significantly different gradients than the observed $+0.1$ dex/kpc gradient of SPT0311-58 E. Short of systematic effects with spatial resolution or metallicity diagnostics, it is unclear how to explain the strong positive gradient observed in SPT0311-58 E.

In summary, the majority of gradients are either relatively flat or strongly negative, regardless of feedback implementation. The population of strong positive gradients seen in observations across redshift can therefore not be easily explained in the scatter of current simulations models.

5. CONCLUSIONS

In this work, we analyze the gas-phase radial metallicity gradients in the modern high redshift ($3 < z \lesssim 11$) cosmological simulations FIRE, SPICE, and Thesan. This suite of models is particularly advantageous because it spans a range of star formation modes – both strongly time-variable (i.e., bursty) and relatively smooth (see Figure 1) – and therefore captures the corresponding diversity in stellar feedback. We construct one dimensional metallicity profiles for each galaxy and fit it with a linear regression (see Figure 2 for examples from each simulation model).

Our key conclusions are as follows:

- We find that metallicity gradients are systematically flatter in bursty (FIRE-2, SPICE Bursty, and Thesan Zoom) than in smooth (SPICE Smooth

and Thesan Box) feedback models (Figure 3). We note that this results is – remarkably – mostly independent of the detailed implementations of each simulation model, and follows nicely from the previous results in EAGLE, Illustris, IllustrisTNG, and SIMBA from Garcia et al. (2025a), suggesting that metallicity gradients are largely robust to modeling assumptions.

- We find that the discrepancy between smooth and bursty feedback models is most clear in massive galaxies ($M_\star > 10^{9.0} M_\odot$; Figure 4). Low mass galaxies do show some level of variation between the different feedback implementations, but the difference is more subtle and would likely be difficult to discriminate within the current observational paradigm.

- We contextualize our results with the first paper in this series (Garcia et al. 2025b), which shows smooth feedback models at $0 \leq z \leq 8$, and recent *JWST*/ALMA observations (Figure 5). We find good agreement between the metallicity gradients in smooth feedback models of this work (Thesan Box and SPICE Smooth) and EAGLE, Illustris, TNG, and SIMBA, suggesting that the strong negative gradients are a highly generic feature of smooth feedback models. Moreover, the agreement between FIRE, SPICE Bursty, and Thesan Zoom suggests that the flat gradients may be a generic feature of bursty feedback models.

- Finally, we find that the recent high redshift gradient observations (Arribas et al. 2024; Vallini et al. 2024; Venturi et al. 2024; Li et al. 2025) tend to align more closely with the gradients from bursty feedback models. In fact, both smooth and bursty models struggle to reproduce strong positive gradients at all (with only $\sim 1.5\%$ of the entire sample having gradients > 0.1 dex/kpc).

Already *JWST* has transformed our understanding of the role of stellar feedback in the early Universe. The results presented in this work and Garcia et al. (2025b) further demonstrate the utility for continued observations of metallicity gradients at high redshift to be constraining for the nature of feedback. Smooth and bursty feedback models make *qualitatively* different predictions for the strength, and evolution, of gradients. A large sample of high resolution observations of galaxies in the first few 100 Myrs of the history of the Universe should provide strong constraints for our understanding of stellar feedback.

REFERENCES

Acharyya, A., Krumholz, M. R., Federrath, C., et al. 2020, MNRAS, 495, 3819, doi: 10.1093/mnras/staa1100

Acharyya, A., Peeples, M. S., Tumlinson, J., et al. 2024, arXiv e-prints, arXiv:2404.06613, doi: 10.48550/arXiv.2404.06613

Acharyya, A., Watson, P. J., Vulcani, B., et al. 2025, arXiv e-prints, arXiv:2508.05335, doi: 10.48550/arXiv.2508.05335

Agertz, O., Teyssier, R., & Moore, B. 2011, MNRAS, 410, 1391, doi: 10.1111/j.1365-2966.2010.17530.x

Anglés-Alcázar, D., Faucher-Giguère, C.-A., Kereš, D., et al. 2017, MNRAS, 470, 4698, doi: 10.1093/mnras/stx1517

Arribas, S., Perna, M., Rodríguez Del Pino, B., et al. 2024, A&A, 688, A146, doi: 10.1051/0004-6361/202348824

Bassini, L., Feldmann, R., Gensior, J., et al. 2024, MNRAS, 532, L14, doi: 10.1093/mnrasl/slae036

Belfiore, F., Maiolino, R., Tremonti, C., et al. 2017, MNRAS, 469, 151, doi: 10.1093/mnras/stx789

Bellardini, M. A., Wetzel, A., Loebman, S. R., et al. 2021, MNRAS, 505, 4586, doi: 10.1093/mnras/stab1606

Bhagwat, A., Costa, T., Ciardi, B., Pakmor, R., & Garaldi, E. 2024, MNRAS, 531, 3406, doi: 10.1093/mnras/stae1125

Brook, C. B., Stinson, G., Gibson, B. K., Wadsley, J., & Quinn, T. 2012, MNRAS, 424, 1275, doi: 10.1111/j.1365-2966.2012.21306.x

Carton, D., Brinchmann, J., Contini, T., et al. 2018, MNRAS, 478, 4293, doi: 10.1093/mnras/sty1343

Ceverino, D., Sánchez Almeida, J., Muñoz Tuñón, C., et al. 2016, MNRAS, 457, 2605, doi: 10.1093/mnras/stw064

Chabrier, G. 2003, PASP, 115, 763, doi: 10.1086/376392

Chan, T. K., Kereš, D., Wetzel, A., et al. 2018, MNRAS, 478, 906, doi: 10.1093/mnras/sty1153

Cochrane, R. K., Katz, H., Begley, R., Hayward, C. C., & Best, P. N. 2025, ApJL, 978, L42, doi: 10.3847/2041-8213/ad9a4d

Cresci, G., Mannucci, F., Maiolino, R., et al. 2010, Nature, 467, 811, doi: 10.1038/nature09451

Curti, M., Maiolino, R., Cirasuolo, M., et al. 2020, MNRAS, 492, 821, doi: 10.1093/mnras/stz3379

Dale, J. E., Bonnell, I. A., Clarke, C. J., & Bate, M. R. 2005, MNRAS, 358, 291, doi: 10.1111/j.1365-2966.2005.08806.x

Danhaive, A. L., Tacchella, S., \"Ubler, H., et al. 2025, arXiv e-prints, arXiv:2503.21863, doi: 10.48550/arXiv.2503.21863

Davé, R., Anglés-Alcázar, D., Narayanan, D., et al. 2019, MNRAS, 486, 2827, doi: 10.1093/mnras/stz937

Doherty, C. L., Gil-Pons, P., Lau, H. H. B., Lattanzio, J. C., & Siess, L. 2014, MNRAS, 437, 195, doi: 10.1093/mnras/stt1877

El-Badry, K., Wetzel, A., Geha, M., et al. 2016, ApJ, 820, 131, doi: 10.3847/0004-637X/820/2/131

El-Badry, K., Quataert, E., Wetzel, A., et al. 2018, MNRAS, 473, 1930, doi: 10.1093/mnras/stx2482

Escala, I., Wetzel, A., Kirby, E. N., et al. 2018, MNRAS, 474, 2194, doi: 10.1093/mnras/stx2858

Evans, Neal J., I., Dunham, M. M., Jørgensen, J. K., et al. 2009, ApJS, 181, 321, doi: 10.1088/0067-0049/181/2/321

Federrath, C., & Klessen, R. S. 2012, ApJ, 761, 156, doi: 10.1088/0004-637X/761/2/156

Feldmann, R., Quataert, E., Faucher-Giguère, C.-A., et al. 2023, MNRAS, 522, 3831, doi: 10.1093/mnras/stad1205

Ferrero, I., Navarro, J. F., Abadi, M. G., et al. 2017, MNRAS, 464, 4736, doi: 10.1093/mnras/stw2691

Fishlock, C. K., Karakas, A. I., Lugaro, M., & Yong, D. 2014, ApJ, 797, 44, doi: 10.1088/0004-637X/797/1/44

Forouhar Moreno, V. J., Helly, J., McGibbon, R., et al. 2025, MNRAS, doi: 10.1093/mnras/staf1478

Förster Schreiber, N. M., Renzini, A., Mancini, C., et al. 2018, ApJS, 238, 21, doi: 10.3847/1538-4365/aadd49

Franchetto, A., Mingozzi, M., Poggianti, B. M., et al. 2021, arXiv e-prints, arXiv:2109.02656. https://arxiv.org/abs/2109.02656

Friedli, D., & Benz, W. 1995, A&A, 301, 649

Friedli, D., Benz, W., & Kennicutt, R. 1994, ApJL, 430, L105, doi: 10.1086/187449

Fujimoto, S., Faisst, A. L., Tsujita, A., et al. 2025, arXiv e-prints, arXiv:2510.16116. https://arxiv.org/abs/2510.16116

Garaldi, E., Kannan, R., Smith, A., et al. 2022, MNRAS, 512, 4909, doi: 10.1093/mnras/stac257

Garcia, A. M., Torrey, P., Hemler, Z. S., et al. 2023, MNRAS, 519, 4716, doi: 10.1093/mnras/stac3749

Garcia, A. M., Torrey, P., Grasha, K., et al. 2024a, MNRAS, 529, 3342, doi: 10.1093/mnras/stae737

Garcia, A. M., Torrey, P., Ellison, S., et al. 2024b, MNRAS, 531, 1398, doi: 10.1093/mnras/stae1252

Garcia, A. M., Torrey, P., Ellison, S. L., et al. 2025a, MNRAS, 536, 119, doi: 10.1093/mnras/stae2587

Garcia, A. M., Torrey, P., Bhagwat, A., et al. 2025b, ApJ, 989, 147, doi: 10.3847/1538-4357/adea51

Garrison-Kimmel, S., Wetzel, A., Bullock, J. S., et al. 2017, MNRAS, 471, 1709, doi: 10.1093/mnras/stx1710

Garrison-Kimmel, S., Hopkins, P. F., Wetzel, A., et al. 2019, MNRAS, 487, 1380, doi: 10.1093/mnras/stz1317

Genel, S., Vogelsberger, M., Springel, V., et al. 2014, MNRAS, 445, 175, doi: 10.1093/mnras/stu1654

Gibson, B. K., Pilkington, K., Brook, C. B., Stinson, G. S., & Bailin, J. 2013, A&A, 554, A47, doi: 10.1051/0004-6361/201321239

Graf, R. L., Wetzel, A., Bailin, J., & Orr, M. E. 2024, arXiv e-prints, arXiv:2410.21377, doi: 10.48550/arXiv.2410.21377

Grasha, K., Chen, Q. H., Battisti, A. J., et al. 2022, ApJ, 929, 118, doi: 10.3847/1538-4357/ac5ab2

Grossi, M., García-Benito, R., Cortesi, A., et al. 2020, MNRAS, 498, 1939, doi: 10.1093/mnras/staa2382

Hemler, Z. S., Torrey, P., Qi, J., et al. 2021, MNRAS, 506, 3024, doi: 10.1093/mnras/stab1803

Hennebelle, P., & Chabrier, G. 2011, ApJL, 743, L29, doi: 10.1088/2041-8205/743/2/L29

Hopkins, P. F. 2015, MNRAS, 450, 53, doi: 10.1093/mnras/stv195

—. 2017, MNRAS, 466, 3387, doi: 10.1093/mnras/stw3306

Hopkins, P. F., Kereš, D., Oñorbe, J., et al. 2014, MNRAS, 445, 581, doi: 10.1093/mnras/stu1738

Hopkins, P. F., Wetzel, A., Kereš, D., et al. 2018, MNRAS, 480, 800, doi: 10.1093/mnras/sty1690

Ivey, L. R., Scholtz, J., Danhaive, A. L., et al. 2025, arXiv e-prints, arXiv:2507.14936, doi: 10.48550/arXiv.2507.14936

Iwamoto, K., Brachwitz, F., Nomoto, K., et al. 1999, ApJS, 125, 439, doi: 10.1086/313278

Izzard, R. G., Tout, C. A., Karakas, A. I., & Pols, O. R. 2004, MNRAS, 350, 407, doi: 10.1111/j.1365-2966.2004.07446.x

Jijina, J., & Adams, F. C. 1996, ApJ, 462, 874, doi: 10.1086/177201

Jones, T., Ellis, R. S., Richard, J., & Jullo, E. 2013, ApJ, 765, 48, doi: 10.1088/0004-637X/765/1/48

Jones, T., Wang, X., Schmidt, K. B., et al. 2015, AJ, 149, 107, doi: 10.1088/0004-6256/149/3/107

Ju, M., Wang, X., Jones, T., et al. 2025, ApJL, 978, L39, doi: 10.3847/2041-8213/ada150

Kannan, R., Garaldi, E., Smith, A., et al. 2022, MNRAS, 511, 4005, doi: 10.1093/mnras/stab3710

Kannan, R., Marinacci, F., Simpson, C. M., Glover, S. C. O., & Hernquist, L. 2020, MNRAS, 491, 2088, doi: 10.1093/mnras/stz3078

Kannan, R., Vogelsberger, M., Marinacci, F., et al. 2019, MNRAS, 485, 117, doi: 10.1093/mnras/stz287

Kannan, R., Puchwein, E., Smith, A., et al. 2025, arXiv e-prints, arXiv:2502.20437, doi: 10.48550/arXiv.2502.20437

Karakas, A. I. 2010, MNRAS, 403, 1413, doi: 10.1111/j.1365-2966.2009.16198.x

Kewley, L. J., Nicholls, D. C., & Sutherland, R. S. 2019, ARA&A, 57, 511, doi: 10.1146/annurev-astro-081817-051832

Knollmann, S. R., & Knebe, A. 2009, ApJS, 182, 608, doi: 10.1088/0067-0049/182/2/608

Kobayashi, C., Umeda, H., Nomoto, K., Tominaga, N., & Ohkubo, T. 2006, ApJ, 653, 1145, doi: 10.1086/508914

Kretschmer, M., & Teyssier, R. 2020, MNRAS, 492, 1385, doi: 10.1093/mnras/stz3495

Kroupa, P. 2002, Science, 295, 82, doi: 10.1126/science.1067524

Lazar, A., Bullock, J. S., Boylan-Kolchin, M., et al. 2020, MNRAS, 497, 2393, doi: 10.1093/mnras/staa2101

Leethochawalit, N., Jones, T. A., Ellis, R. S., et al. 2016, ApJ, 820, 84, doi: 10.3847/0004-637X/820/2/84

Leitherer, C., Ekström, S., Meynet, G., et al. 2014, ApJS, 212, 14, doi: 10.1088/0067-0049/212/1/14

Leitherer, C., Schaerer, D., Goldader, J. D., et al. 1999, ApJS, 123, 3, doi: 10.1086/313233

Li, Z., Wang, X., Cai, Z., et al. 2022, ApJL, 929, L8, doi: 10.3847/2041-8213/ac626f

Li, Z., Cai, Z., Wang, X., et al. 2025, arXiv e-prints, arXiv:2506.12129, doi: 10.48550/arXiv.2506.12129

Looser, T. J., D'Eugenio, F., Maiolino, R., et al. 2024, Nature, 629, 53, doi: 10.1038/s41586-024-07227-0

Lopez, L. A., Krumholz, M. R., Bolatto, A. D., Prochaska, J. X., & Ramirez-Ruiz, E. 2011, ApJ, 731, 91, doi: 10.1088/0004-637X/731/2/91

Ma, X., Hopkins, P. F., Feldmann, R., et al. 2017, MNRAS, 466, 4780, doi: 10.1093/mnras/stx034

Ma, X., Quataert, E., Wetzel, A., et al. 2020, MNRAS, 498, 2001, doi: 10.1093/mnras/staa2404

Ma, X., Hopkins, P. F., Garrison-Kimmel, S., et al. 2018, MNRAS, 478, 1694, doi: 10.1093/mnras/sty1024

Ma, X., Hayward, C. C., Casey, C. M., et al. 2019, MNRAS, 487, 1844, doi: 10.1093/mnras/stz1324

Maiolino, R., & Mannucci, F. 2019, A&A Rv, 27, 3, doi: 10.1007/s00159-018-0112-2

Mannucci, F., Della Valle, M., & Panagia, N. 2006, MNRAS, 370, 773, doi: 10.1111/j.1365-2966.2006.10501.x

Marigo, P. 2001, A&A, 370, 194, doi: 10.1051/0004-6361:20000247

Marinacci, F., Sales, L. V., Vogelsberger, M., Torrey, P., & Springel, V. 2019, MNRAS, 489, 4233, doi: 10.1093/mnras/stz2391

Marszewski, A., Faucher-Giguère, C.-A., Feldmann, R., & Sun, G. 2025, ApJL, 991, L4, doi: 10.3847/2041-8213/adf74b

McClymont, W., Tacchella, S., Smith, A., et al. 2025a, arXiv e-prints, arXiv:2503.04894, doi: 10.48550/arXiv.2503.04894

—. 2025b, arXiv e-prints, arXiv:2507.08787, doi: 10.48550/arXiv.2507.08787

McKinnon, R., Torrey, P., & Vogelsberger, M. 2016, MNRAS, 457, 3775, doi: 10.1093/mnras/stw253

McKinnon, R., Torrey, P., Vogelsberger, M., Hayward, C. C., & Marinacci, F. 2017, MNRAS, 468, 1505, doi: 10.1093/mnras/stx467

Mostow, O., Torrey, P., Rose, J., et al. 2024, arXiv e-prints, arXiv:2412.09566. https://arxiv.org/abs/2412.09566

Muratov, A. L., Kereš, D., Faucher-Giguère, C.-A., et al. 2015, MNRAS, 454, 2691, doi: 10.1093/mnras/stv2126

—. 2017, MNRAS, 468, 4170, doi: 10.1093/mnras/stx667

Narayanan, D., Stark, D. P., Finkelstein, S. L., et al. 2024a, arXiv e-prints, arXiv:2408.13312, doi: 10.48550/arXiv.2408.13312

Narayanan, D., Lower, S., Torrey, P., et al. 2024b, ApJ, 961, 73, doi: 10.3847/1538-4357/ad0966

Nelson, E. J., Tacchella, S., Diemer, B., et al. 2021, MNRAS, 508, 219, doi: 10.1093/mnras/stab2131

Nomoto, K., Iwamoto, K., Nakasato, N., et al. 1997, NuPhA, 621, 467, doi: 10.1016/S0375-9474(97)00291-1

Nomoto, K., Tominaga, N., Umeda, H., Kobayashi, C., & Maeda, K. 2006, NuPhA, 777, 424, doi: 10.1016/j.nuclphysa.2006.05.008

Orr, M. E., Burkhart, B., Wetzel, A., et al. 2023, MNRAS, 521, 3708, doi: 10.1093/mnras/stad676

Pandya, V., Fielding, D. B., Anglés-Alcázar, D., et al. 2021, MNRAS, 508, 2979, doi: 10.1093/mnras/stab2714

Péroux, C., & Howk, J. C. 2020, ARA&A, 58, 363, doi: 10.1146/annurev-astro-021820-120014

Pilkington, K., Gibson, B. K., Brook, C. B., et al. 2012, MNRAS, 425, 969, doi: 10.1111/j.1365-2966.2012.21353.x

Pillepich, A., Springel, V., Nelson, D., et al. 2018, MNRAS, 473, 4077, doi: 10.1093/mnras/stx2656

Pontzen, A., & Governato, F. 2012, MNRAS, 421, 3464, doi: 10.1111/j.1365-2966.2012.20571.x

Portinari, L., Chiosi, C., & Bressan, A. 1998, A&A, 334, 505, doi: 10.48550/arXiv.astro-ph/9711337

Prantzos, N., & Boissier, S. 2000, MNRAS, 313, 338, doi: 10.1046/j.1365-8711.2000.03228.x

Pérez, E., Cid Fernandes, R., González Delgado, R. M., et al. 2013, ApJL, 764, L1, doi: 10.1088/2041-8205/764/1/L1

Queyrel, J., Contini, T., Kissler-Patig, M., et al. 2012, A&A, 539, A93, doi: 10.1051/0004-6361/201117718

Quillen, A. C., Thorndike, S. L., Cunningham, A., et al. 2005, ApJ, 632, 941, doi: 10.1086/444410

Read, J. I., & Gilmore, G. 2005, MNRAS, 356, 107, doi: 10.1111/j.1365-2966.2004.08424.x

Rodríguez Del Pino, B., Perna, M., Arribas, S., et al. 2024, A&A, 684, A187, doi: 10.1051/0004-6361/202348057

Rosdahl, J., Blaizot, J., Aubert, D., Stranex, T., & Teyssier, R. 2013, MNRAS, 436, 2188, doi: 10.1093/mnras/stt1722

Rosdahl, J., & Teyssier, R. 2015, MNRAS, 449, 4380, doi: 10.1093/mnras/stv567

Rupke, D. S. N., Kewley, L. J., & Barnes, J. E. 2010a, ApJL, 710, L156, doi: 10.1088/2041-8205/710/2/L156

Rupke, D. S. N., Kewley, L. J., & Chien, L. H. 2010b, ApJ, 723, 1255, doi: 10.1088/0004-637X/723/2/1255

Samuel, J., Wetzel, A., Tollerud, E., et al. 2020, MNRAS, 491, 1471, doi: 10.1093/mnras/stz3054

Sánchez, S. F., Rosales-Ortega, F. F., Marino, R. A., et al. 2012, A&A, 546, A2, doi: 10.1051/0004-6361/201219578

Sánchez, S. F., Rosales-Ortega, F. F., Jungwiert, B., et al. 2013, A&A, 554, A58, doi: 10.1051/0004-6361/201220669

Sánchez, S. F., Rosales-Ortega, F. F., Iglesias-Páramo, J., et al. 2014, A&A, 563, A49, doi: 10.1051/0004-6361/201322343

Sánchez-Menguiano, L., Sánchez, S. F., Pérez, I., et al. 2016, A&A, 587, A70, doi: 10.1051/0004-6361/201527450

Schaye, J., & Dalla Vecchia, C. 2008, MNRAS, 383, 1210, doi: 10.1111/j.1365-2966.2007.12639.x

Schaye, J., Crain, R. A., Bower, R. G., et al. 2015, MNRAS, 446, 521, doi: 10.1093/mnras/stu2058

Schaye, J., Chaikin, E., Schaller, M., et al. 2025, arXiv e-prints, arXiv:2508.21126, doi: 10.48550/arXiv.2508.21126

Schmidt, W., Niemeyer, J. C., Hillebrandt, W., & Röpke, F. K. 2006, A&A, 450, 283, doi: 10.1051/0004-6361:20053618

Searle, L. 1971, ApJ, 168, 327, doi: 10.1086/151090

Shen, X., Vogelsberger, M., Boylan-Kolchin, M., Tacchella, S., & Kannan, R. 2023, MNRAS, 525, 3254, doi: 10.1093/mnras/stad2508

Shen, X., Vogelsberger, M., Boylan-Kolchin, M., Tacchella, S., & Naidu, R. P. 2024a, MNRAS, 533, 3923, doi: 10.1093/mnras/stae1932

Shen, X., Vogelsberger, M., Borrow, J., et al. 2024b, MNRAS, 534, 1433, doi: 10.1093/mnras/stae2156

Shen, X., Kannan, R., Puchwein, E., et al. 2025, arXiv e-prints, arXiv:2503.01949, doi: 10.48550/arXiv.2503.01949

Simons, R. C., Papovich, C., Momcheva, I., et al. 2021, ApJ, 923, 203, doi: 10.3847/1538-4357/ac28f4

Smith, A., Kannan, R., Garaldi, E., et al. 2022, MNRAS, 512, 3243, doi: 10.1093/mnras/stac713

Sparre, M., Hayward, C. C., Feldmann, R., et al. 2017, MNRAS, 466, 88, doi: 10.1093/mnras/stw3011

Sparre, M., Hayward, C. C., Springel, V., et al. 2015, MNRAS, 447, 3548, doi: 10.1093/mnras/stu2713

Springel, V. 2010, MNRAS, 401, 791, doi: 10.1111/j.1365-2966.2009.15715.x

Springel, V., & Hernquist, L. 2003, MNRAS, 339, 289, doi: 10.1046/j.1365-8711.2003.06206.x

Springel, V., White, M., & Hernquist, L. 2001, ApJ, 549, 681, doi: 10.1086/319473

Stanghellini, L., Magrini, L., & Casasola, V. 2015, ApJ, 812, 39, doi: 10.1088/0004-637X/812/1/39

Stinson, G. S., Bailin, J., Couchman, H., et al. 2010, MNRAS, 408, 812, doi: 10.1111/j.1365-2966.2010.17187.x

Su, K.-Y., Hopkins, P. F., Hayward, C. C., et al. 2017, MNRAS, 471, 144, doi: 10.1093/mnras/stx1463

Sun, G., Faucher-Giguère, C.-A., Hayward, C. C., et al. 2023, ApJL, 955, L35, doi: 10.3847/2041-8213/acf85a

Sun, X., Wang, X., Ma, X., et al. 2024, arXiv e-prints, arXiv:2409.09290, doi: 10.48550/arXiv.2409.09290

Swinbank, A. M., Sobral, D., Smail, I., et al. 2012, MNRAS, 426, 935, doi: 10.1111/j.1365-2966.2012.21774.x

Tapia-Contreras, B., Tissera, P. B., Sillero, E., et al. 2025, A&A, 700, A69, doi: 10.1051/0004-6361/202554013

Teyssier, R. 2002, A&A, 385, 337, doi: 10.1051/0004-6361:20011817

Tissera, P. B., Rosas-Guevara, Y., Bower, R. G., et al. 2019, MNRAS, 482, 2208, doi: 10.1093/mnras/sty2817

Tissera, P. B., Rosas-Guevara, Y., Sillero, E., et al. 2022, MNRAS, 511, 1667, doi: 10.1093/mnras/stab3644

Torrey, P., Cox, T. J., Kewley, L., & Hernquist, L. 2012, ApJ, 746, 108, doi: 10.1088/0004-637X/746/1/108

Torrey, P., Hopkins, P. F., Faucher-Giguère, C.-A., et al. 2017, MNRAS, 467, 2301, doi: 10.1093/mnras/stx254

Torrey, P., Vogelsberger, M., Marinacci, F., et al. 2019, MNRAS, 484, 5587, doi: 10.1093/mnras/stz243

Tripodi, R., D'Eugenio, F., Maiolino, R., et al. 2024, A&A, 692, A184, doi: 10.1051/0004-6361/202449980

Troncoso, P., Maiolino, R., Sommariva, V., et al. 2014, A&A, 563, A58, doi: 10.1051/0004-6361/201322099

Tumlinson, J., Peeples, M. S., & Werk, J. K. 2017, ARA&A, 55, 389, doi: 10.1146/annurev-astro-091916-055240

Valé, G., Lara-López, M. A., Valerdi, M., et al. 2025, A&A, 701, A226, doi: 10.1051/0004-6361/202553818

Vallini, L., Witstok, J., Sommovigo, L., et al. 2024, MNRAS, 527, 10, doi: 10.1093/mnras/stad3150

van den Hoek, L. B., & Groenewegen, M. A. T. 1997, A&AS, 123, 305, doi: 10.1051/aas:1997162

Venturi, G., Carniani, S., Parlanti, E., et al. 2024, arXiv e-prints, arXiv:2403.03977, doi: 10.48550/arXiv.2403.03977

Vogelsberger, M., Genel, S., Sijacki, D., et al. 2013, MNRAS, 436, 3031, doi: 10.1093/mnras/stt1789

Vogelsberger, M., Marinacci, F., Torrey, P., & Puchwein, E. 2020, Nature Reviews Physics, 2, 42, doi: 10.1038/s42254-019-0127-2

Vogelsberger, M., Genel, S., Springel, V., et al. 2014, MNRAS, 444, 1518, doi: 10.1093/mnras/stu1536

Wang, X., Jones, T. A., Treu, T., et al. 2017, ApJ, 837, 89, doi: 10.3847/1538-4357/aa603c

—. 2019, ApJ, 882, 94, doi: 10.3847/1538-4357/ab3861

—. 2020, ApJ, 900, 183, doi: 10.3847/1538-4357/abacce

Wang, X., Jones, T., Vulcani, B., et al. 2022, ApJL, 938, L16, doi: 10.3847/2041-8213/ac959e

Wang, Z., Shen, X., Vogelsberger, M., et al. 2025, arXiv e-prints, arXiv:2505.05554, doi: 10.48550/arXiv.2505.05554

Weinberger, R., Springel, V., Hernquist, L., et al. 2017, MNRAS, 465, 3291, doi: 10.1093/mnras/stw2944

Weinberger, R., Springel, V., Pakmor, R., et al. 2018, MNRAS, 479, 4056, doi: 10.1093/mnras/sty1733

Wetzel, A., Hayward, C. C., Sanderson, R. E., et al. 2023, ApJS, 265, 44, doi: 10.3847/1538-4365/acb99a

Wetzel, A., Samuel, J., Gandhi, P. J., et al. 2025, arXiv e-prints, arXiv:2508.06608, doi: 10.48550/arXiv.2508.06608

Wetzel, A. R., Hopkins, P. F., Kim, J.-h., et al. 2016, ApJL, 827, L23, doi: 10.3847/2041-8205/827/2/L23

Witten, C., McClymont, W., Laporte, N., et al. 2025, MNRAS, 537, 112, doi: 10.1093/mnras/staf001

Wuyts, E., Wisnioski, E., Fossati, M., et al. 2016, ApJ, 827, 74, doi: 10.3847/0004-637X/827/1/74

Yorke, H. W., Tenorio-Tagle, G., Bodenheimer, P., & Rozyczka, M. 1989, A&A, 216, 207

Yuan, T. T., Kewley, L. J., & Rich, J. 2013, ApJ, 767, 106, doi: 10.1088/0004-637X/767/2/106